UDK 621.791.725:691.714:004.942
Original scientific article/Izvirni znanstveni članek

ISSN 1580-2949
Mater. Tehnol.

OPTIMIZATION OF LASER SPOT WELDING PARAMETERS FOR 304 STAINLESS STEEL THIN SHEETS USING NUMERICAL SIMULATION

OPTIMIZACIJA PARAMETROV LASERSKEGA TOČKOVNEGA VARJENJA TANKIH PLOČEVIN IZ NERJAVNEGA JEKLA TIPA 304 Z UPORABO NUMERIČNE SIMULACIJE

Jin Peng[1,2,3*], Junhai Xia[2], Shihua Xie[2], Jie Chen[2], Lei Zhang[1*], Yongtao Jiu[1,6], Yujia Li[1], Xiaokai Yu[4], Xiangyun Zhang[4], Nannan Chen[5]

[1]Ningbo Intelligent Machine Tool Research Institute Co., Ltd., China National Machinery Institute Group, Ningbo 315700, China
[2]School of Materials Science and Engineering, North China University of Water Resources and Electric Power, Zhengzhou, Henan 450045, China
[3]Henan Engineering Research Center on Special Materials and Applications of Water Conservancy and Hydropower Engineering, Zhengzhou, Henan 450045, China
[4]Luoyang Bearing Research Institute Co., Ltd., Luoyang 471039, China
[5]School of Materials Science and Engineering, Shanghai Jiao Tong University, No. 800, Dong Chuan Road, Shanghai 200240, China
[6]Ningbo Key Laboratory of Manufacturing Technology and Equipment of Core Functional Prats for Advanced CNC Machine, Ningbo 315700, China

Prejem rokopisa – received: 2025-06-08; sprejem za objavo – accepted for publication: 2025-09-18

doi:10.17222/mit.2025.1475

Laser spot welding of stainless steel is widely used for connecting vehicle body structures and electronic components. In this study, numerical simulation of laser spot welding was conducted on lap joints of 304 austenitic stainless steel thin plates measuring 120 × 80 × 0.8 mm. The equivalent stress and total deformation of the welded joints under different welding sequences and fixture clamping forces were investigated, and the stress and deformation around the weld spots were characterized. The results demonstrate that at a laser power of 1300 W, the equivalent stress after welding with the sequence (1-4-3-6-2-5) reaches a minimum value of the maximum equivalent stress of 421.87 MPa, indicating the optimal welding sequence. Under the optimal welding sequence, when the clamping forces on both sides are 100 N, the equivalent stress and total deformation reach the lowest values of 421.87 MPa and 0.27 mm, respectively, representing the optimal fixture clamping forces. These findings provide guidance for optimizing the laser spot welding process in industrial applications.

Keywords: numerical simulation, stainless steel, thin plate, laser spot welding, process optimization

Llasersko točkovno varjenje nerjavnih jekel se množično uporablja za spajanje delov avtomobilskih šasij (konstrukcij) in elektronskih komponent. V tem članku avtorji opisujejo numerično simulacijo prekrivnih spojev sestavljenih iz tankih nerjavnih pločevin, dimenzij 120 mm × 80 mm × 0,8 mm. Avtorji so za svoje preizkuse izbrali nerjavno austenitno Cr-Ni jeklo vrste 304. Ugotavljali so ekvivalentno napetost in totalno (celokupno) deformacijo ter napetost in deformacijo v okolici točkovnih zvarov pri različnih sekvencah (zaporedjih) varjenja in silah medsebojnega vpenjanja (pričvrstitve) pločevin. Rezultati raziskave so pokazali, pri uporabljeni moči laserja 1300 W, da je imela ekvivalentna napetost po varjenju s sekvenco 1-4-3-6-2-5 najmanjšo vrednost maksimalne ekvivalentne napetosti (421,87 MPa), kar pomeni optimalno izbrano sekvenco varjenja. Pri optimalnih pogojih varjenja so avtorji uporabili obojestransko pričvrstitev s silo 100 N. Pri teh pogojih sta bili doseženi najnižji vrednosti za ekvivalentno napetost in celokupno deformacijo in sicer 421,87 MPa oziroma 0,27 mm. Avtorji v zaključkih poudarjajo, da rezultati in ugotovitve te raziskave lahko služijo kot vodilo za optimiziranje postopka laserskega točkovnega varjenja pri različnih industrijskih aplikacijah.

Ključne besede: numerična simulacija, nerjavno jeklo, tanka pločevina, lasersko točkovno varjenje, optimiziranje procesa

1 INTRODUCTION

The 304 austenitic stainless steel exhibits excellent corrosion resistance, weldability, and machinability. Due to these properties, it is widely used for hydrogen storage tanks, oil pipelines, and the aerospace sector.[1–3] In the context of energy conservation and emission reduction, lightweight materials are increasingly favored due to their lower production costs and reduced energy consumption. When performance requirements are met, lightweight design is a key objective in component manufacturing. 304 austenitic stainless steel thin sheets are characterized by high strength and corrosion resistance. They are widely used in the manufacture of components for medical equipment, precision instruments, and other applications with stringent material requirements.[4,5]

Numerous studies have been conducted on the joining processes of 304 stainless steel. Mekonone et al.[6] performed gas tungsten arc welding (TIG) on 5-mm-thick 304L stainless steel and optimized the welding parameters. Zhou et al.[7] conducted metal active gas welding (MAG) on 3-mm-thick austenitic stainless steel,

*Corresponding author's e-mail:
pengjin1985120@163.com (Jin Peng)

demonstrating that ferrite morphology affects the weld seam's hydrogen embrittlement resistance. Sridhar et al.[8] implemented double-sided submerged arc welding on 12-mm-thick 304 austenitic stainless steel, observing that increased welding current enhanced tensile properties and resulted in ductile fracture characteristics. These studies collectively demonstrate that traditional arc welding is seldom used for joining 304 stainless steel thin-plate components (<1 mm), mainly because the high heat input in arc fusion welding often causes burn-through and induces post-welding deformation in thin sheets. Such deformations and defects compromise dimensional accuracy and adversely affect assembly quality and service performance.[9–11]

Laser spot welding is an advanced joining technique characterized by its high efficiency and precision, utilizing a concentrated high-energy laser beam as the heat source.[12] Compared to conventional arc welding, laser spot welding demonstrates superior performance, including reduced heat input, minimized heat-affected zone (HAZ), and significantly reduced stress concentration and deformation in welded joints.[13–15] The welding spots in laser spot welding typically range within several hundred micrometers, making it ideal for precision welding of ultra-thin materials and micro-scale components.[12] Wu et al.[16] used nanosecond pulsed laser welding to join 0.1-mm-thick 304 stainless steel and 1-mm-thick AZ31B magnesium alloy, achieving good bonding between the plates. Allen et al.[17] used laser spot welding to connect 316 stainless steel (381 μm) and 6061 aluminum alloy (635 μm) in a lap joint, measuring the keyhole depth and absorption rate. Lapsanska et al.[18] performed laser spot welding on 0.6-mm-thick 304 stainless steel plates, studying how laser energy affects the weld diameter and surface roughness. These studies show that laser spot welding can be used to weld stainless steel plates thinner than 1 mm.

However, relying exclusively on physical welding experiments for process optimization is both time-intensive and resource-demanding in terms of materials and costs. Additionally, capturing the dynamic variations in temperature fields, stress fields, and deformation during the welding process remains challenging.[19,20] Numerical simulation has emerged as a prevalent approach for laser welding research, offering advantages including cost-effectiveness, efficiency, precision, and visualizability.[21–23] Zarei et al.[24] simulated laser welding of AISI1060 with both austenitic 304 and ferritic 420 stainless steels, demonstrating good agreement between simulation and experimental results. Danielewski et al.[25] employed numerical simulation to optimize the welding configuration for lap joints between 316L austenitic stainless steel and S355J2 low-carbon steel. These findings confirm that numerical simulation can effectively replicate actual welding processes and facilitate process optimization.

The spot welding process of stainless steel is extensively employed in the manufacturing of automotive body structures.[26,27] Despite these widespread applications, there is currently a lack of reported studies focusing on the optimization of laser spot welding parameters, specifically the welding sequence and fixture clamping force, for 304 austenitic stainless steel thin plates using the numerical simulation technology. To address this gap, this study employs Simufact Welding software to conduct numerical simulation of laser spot welding for 304 stainless steel thin-plate lap joints. The primary objective is to examine joint deformation and residual stress under varying welding sequences and fixture clamping conditions. The optimized laser spot welding parameters derived from this study provide a theoretical foundation and practical guidance for industrial manufacturing applications.

2 EXPERIMENTAL MATERIAL

The experimental material used in this study comprised 304 austenitic stainless steel (0Cr18Ni9) plates, with dimensions of 120 (length) × 80 (width) × 0.8 mm (thickness). The chemical composition of 304 austenitic stainless steel is provided in **Table 1**. The room-temperature mechanical properties of 304 austenitic stainless steel are summarized in **Table 2**.

Table 1: Chemical composition (*w*/%) of 304 austenitic stainless steel[28]

Element	C	Si	Mn	Cr	Fe	Ni
Comp. (*w*/%)	0.05	0.42	0.79	17.27	Bal.	8.14

Table 2: Room-temperature mechanical properties of 304 austenitic stainless steel[28]

Property	Elastic modulus (GPa)	Yield strength (MPa)	Tensile strength (MPa)	Elongation (%)	Reduction of area (%)
Value	209	240	696	63	76

3 NUMERICAL SIMULATION METHODOLOGY

3.1 Finite-element-model development and mesh generation

A three-dimensional geometric model of the lap joint was created using the commercial modeling software Creo Parametric 8.0. The model dimensions were set to (120 × 80 × 0.8) mm. The welded joint configuration comprised two identical 304 austenitic stainless steel plates arranged in an overlapping configuration. The lap joint had a total overlap length of 60 mm.

After constructing the geometric model of the lap joint, Hyper Mesh software was used to generate the mesh for the model. In this study, the hexahedral mesh was selected as the mesh type. The mesh size was graded from 4 × 4 mm at both end regions of the lap joint, progressing to 2 × 2 mm in the central seam area, and further refined to 1 × 1 mm at the welding spot zone. The final mesh configuration consisted of 42,912 elements.

3.2 Heat source model

During laser welding, the energy distribution inside the workpiece is non-uniform, gradually decreasing with increasing depth.[29] The conical heat source model (**Figure 1**) consists of two parts: a planar Gaussian heat source model in the upper region and a rotating body heat source model in the lower region. In terms of energy distribution, the top of the heat source exhibits the maximum energy density, while the root radius exhibits the minimum energy density. This aligns closely with the energy distribution in actual laser welding. This heat source model is widely used in laser welding.[30–32]

The total power Q of the conical heat source is given by:

$$Q = \eta P \tag{1}$$

The energy density $q(r,z)$ at a radial distance r from the center on a plane at height z can be expressed as follows[33]:

$$q(r,z) = \frac{9\eta P e^3}{\pi H(e^3-1)\left(r_e^2 + r_e r_i + r_i^2\right)} \exp\left(-\frac{3r^2}{r_0^2}\right) \tag{2}$$

$$r_0(z) = r_e + \frac{r_i - r_e}{z_i + z_e}(z - z_e) \tag{3}$$

Here, η represents the material's absorption efficiency of the laser, P denotes the laser power, and H is the total height of the heat source. $r_0(z)$ defines the maximum effective radius on the plane at height z, where r_e and r_i are the upper and lower radii of the cone, respectively, and z_e and z_i are the height parameters of the cone.

3.3 Governing equation and boundary condition

In the laser spot welding process, the governing equations for mass, momentum, and energy conservation are as follows:[34,35]

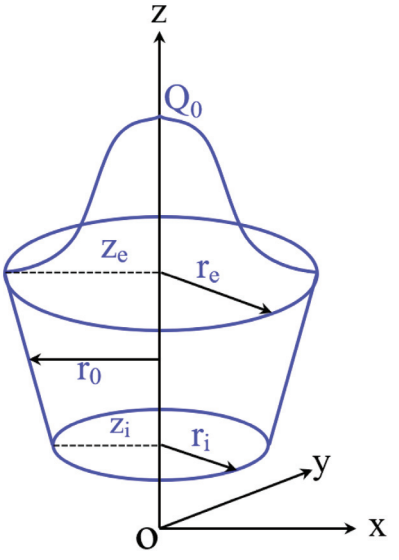

Figure 1: Conical heat source model[33]

Mass conservation equation:

$$\nabla(\rho\vec{U}) = 0 \tag{4}$$

Momentum equation:

$$\frac{\partial(\rho\vec{U})}{\partial t} + \nabla(\rho\vec{U}\vec{U}) = -\nabla P + \nabla(\mu\nabla\vec{U}) + \rho\vec{g} - \frac{\mu}{K}(\vec{U}) \tag{5}$$

Energy equation:

$$\frac{\partial(\rho H)}{\partial t} + \nabla(\rho\vec{U}H) = \nabla(k\nabla T) + h(t)q_v \tag{6}$$

Here, K, μ, $\vec{g}$, p, $\vec{U}$, t, ρ are Darcy resistance coefficient, dynamic viscosity, gravity acceleration vector, pressure, velocity vector, time and density, respectively; k represents the thermal conductivity, H is the total enthalpy, T is the temperature and $h(t)$ is the laser welding coefficient.

During welding heat transfer, the transient temperature field depends on time t and spatial coordinates (x, y, z), governed by the nonlinear heat conduction equation:[36]

$$\rho c\left[\frac{\partial T}{\partial t} + (-v)\frac{\partial T}{\partial y}\right] = \frac{\partial}{\partial x}\left(k\frac{\partial T}{\partial x}\right) + \\ + \frac{\partial}{\partial y}\left(k\frac{\partial T}{\partial y}\right) + \frac{\partial}{\partial z}\left(k\frac{\partial T}{\partial x}z\right) + Q_v(x,y,z) \tag{7}$$

For laser spot welding where workpiece velocity $v = 0$, the governing heat conduction equation simplifies to:

$$\rho c\left[\frac{\partial T}{\partial t}\right] = \frac{\partial}{\partial x}\left(k\frac{\partial T}{\partial x}\right) + \frac{\partial}{\partial y}\left(k\frac{\partial T}{\partial y}\right) + \\ + \frac{\partial}{\partial z}\left(k\frac{\partial T}{\partial x}z\right) + Q_v(x,y,z) \tag{8}$$

Among them, Q_v is the volume heat source term that varies with the beam power and welding speed while c is specific heat.

The natural boundary condition is given by:[36]

$$k_n\left(\frac{\partial T}{\partial n}\right) - q + h(T - T_0) + \sigma\varepsilon(T^4 - T_0^4) = 0 \tag{9}$$

Here, k_n is the thermal conductivity perpendicular to the surface of the welded part (W/m·K), q is the heat flux applied to the surface due to the external heat source (W/m^2), h is the convective heat transfer coefficient (W/m^2·K), σ is the Stefan-Boltzmann constant for radiation (5.67×10^{-8} W/m^2·K^4), and ε is the emissivity.

3.4 Thermal properties of materials

Some thermophysical property parameters of 304 austenitic stainless steel are listed in **Table 3**. Some of them are temperature-dependent and vary with temperature. They were calculated as a function of temperature using JMatPro software. This software utilizes the chemical composition of 304 stainless steel (**Table 1**) and a phase diagram calculation method based on equilibrium

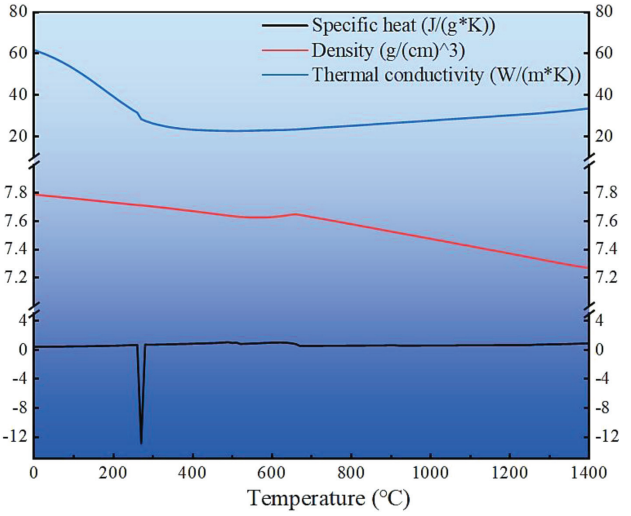

Figure 2: Temperature-dependent variations in thermophysical properties of 304 austenitic stainless steel

phase diagrams to compute and analyze the material's thermophysical properties.[37] The temperature-dependent variations of density, thermal conductivity, and specific heat capacity are illustrated in **Figure 2**.

In 304 austenitic stainless steel, a phase transformation from austenite to martensite can occur during the cooling phase of welding. However, in the present study, the martensitic transformation is typically minimal due to the extremely high heating and cooling rates inherent to laser spot welding. In line with the methodology of Huang et al.,[38] phase transformation and fluid flow were neglected in the numerical simulations to simplify the model and enhance the computational efficiency.

Table 3: Thermophysical property parameters of 304 austenitic stainless steel[39]

Physical property	Symbol	Unit	Value
Solidus temperature	T_s	K	1697
Liquidus temperature	T_L	K	1727
Latent heat of vaporization	L_v	J·kg^{-1}	2×10^5
aautoLatent heat of fusion	L	J·kg^{-1}	246

3.5 Validation of the thermal source model

In this study, the numerical simulations employed the conical heat source model detailed in Section 3.2. Key parameters for the surface Gaussian heat source include the disc radius (r) and surface heat source depth (d_0). For the conical volume heat source, the key parameters are the upper radius (r_u), lower radius (r_l), and depth (d). A single-point laser spot welding experiment was conducted using a CO_2 laser at a laser power of 1300 W. The morphology of the welded spot is shown in **Figure 3**, with a molten pool radius of 1.75 mm. In the Simufact Welding software, the conical heat source model parameters listed in **Table 4** were applied at a laser power of 1300 W, yielding a simulated spot radius of 1.72 mm. The error between the simulated and actual spot radii is

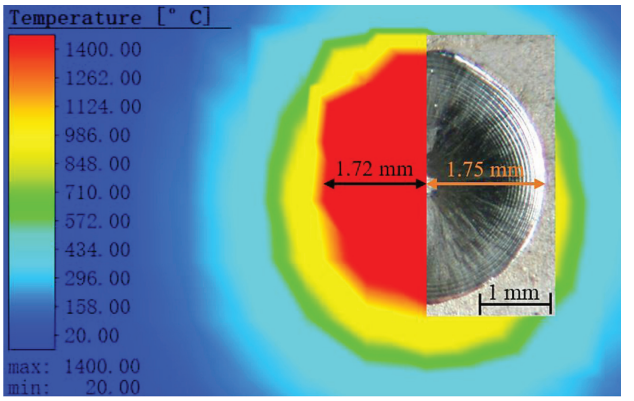

Figure 3: Comparative analysis of experimental and simulated weld dimensions and profiles

only 1.71 %, demonstrating excellent agreement between the simulation results and experimental observations.

Table 4: Optimized parameters of the conical heat source model

Parameter	r	d_0	r_u	r_l	d
Value (mm)	0.5	0.1	0.5	0.1	1.6

3.6 Welding spots and sequence design

Based on the single-point laser spot welding described above, a six-point continuous laser spot welding process was designed. This was done to investigate the influence of welding sequence on post-welding equivalent stress and total deformation. Two rows of spot welds were welded in parallel on the surface of the test piece, with three spot welds in each row. The distance between adjacent spot welds, as well as between the outermost spot welds and the edge of the test piece, was 20 mm, while the distance between the two rows of spot welds was also 20 mm. To facilitate the subsequent planning of the welding sequence, each spot weld was numbered in the Simufact Welding software, as illustrated in **Figure 4**.

This laser spot welding simulation experiment for thin plates investigated the influence of twelve different welding sequences on the stress and strain of the welded

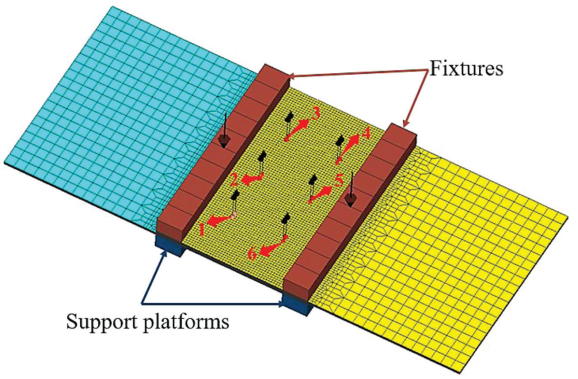

Figure 4: Numbering diagram of spot welds on the lap joint of 304 stainless steel

joints. The sequence in **Table 5** represents the welding order of the 6 welding spots, where the first number indicates the first welded spot and the last number indicates the final welded spot. The laser power was maintained at 1300 W, with each welding spot having a welding time of 0.3 s. The clamping force of the clamps on both the left and right sides was set to 100 N.

Table 5: Welding sequence configurations in laser spot welding simulations

Group	Welding sequence
1	1-2-3-4-5-6
2	1-2-3-6-5-4
3	1-3-2-6-4-5
4	1-3-2-4-6-5
5	2-1-3-5-6-4
6	1-6-3-4-2-5
7	1-4-3-6-2-5
8	1-4-3-6-5-2
9	1-4-6-3-2-5
10	1-4-6-3-5-2
11	2-5-1-6-3-4
12	2-5-1-3-6-4

4 RESULTS AND DISCUSSION

4.1 Comparative analysis of simulation results for laser spot welding with different welding sequences

Laser spot welding processes with twelve different welding sequences (**Table 5**) were simulated using the Simufact Welding software. Simulation results for equivalent stress are presented in **Figure 5**. As shown in this figure, the equivalent stress is predominantly distributed in the lap joint region after welding, while stress values in the areas outside the lap joint are significantly lower. The equivalent stress at the center of the laser spot weld exceeds 420 MPa, indicating the region of a maximum stress concentration in the welded component. The equivalent stress distribution nephogram showed an approximately symmetrical pattern about the central axis of the welded component.

Welding residual stress can accelerate the propagation of cracks in materials. It also reduces the fatigue strength and corrosion resistance of materials, leading to material cracking and shortening their service life.[40–42] The maximum equivalent stress values for different groups were statistically analyzed. As shown in **Fig-**

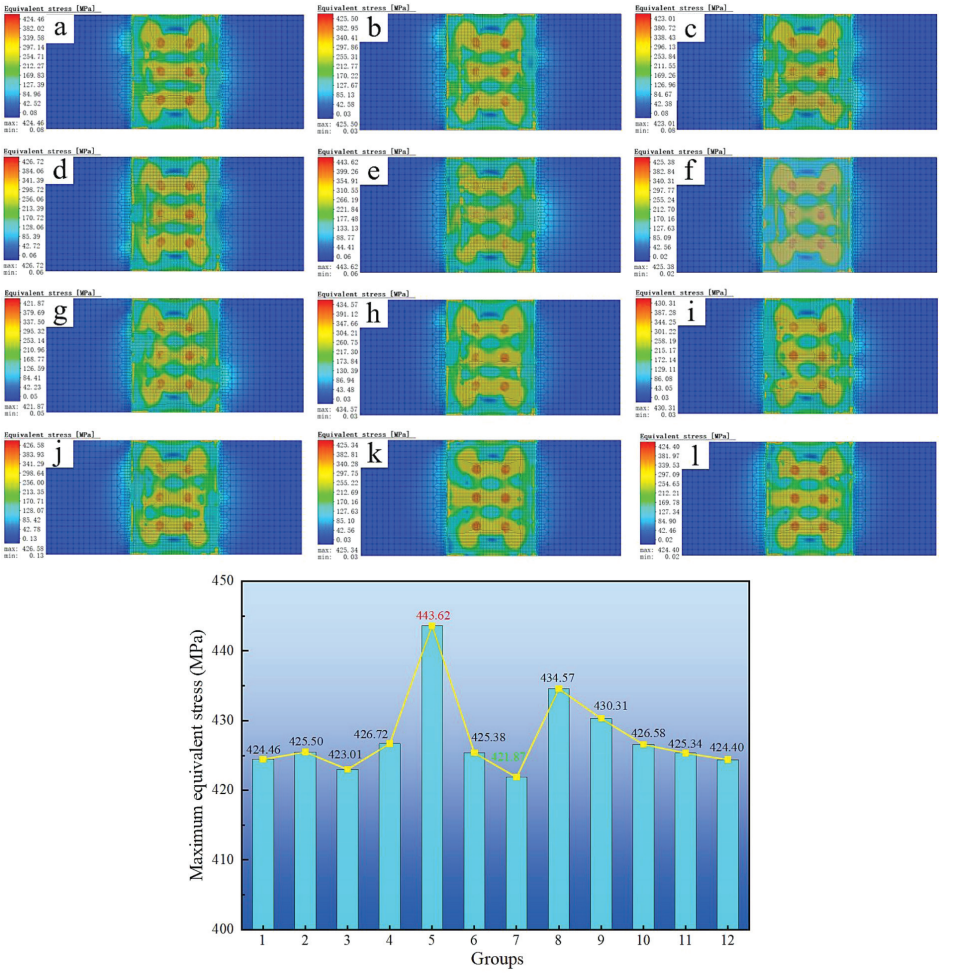

Figure 5: Distribution of equivalent stress from numerical simulations: (a-l) corresponding results for experimental Groups 1–12, respectively, and the statistics of the maximum equivalent stress

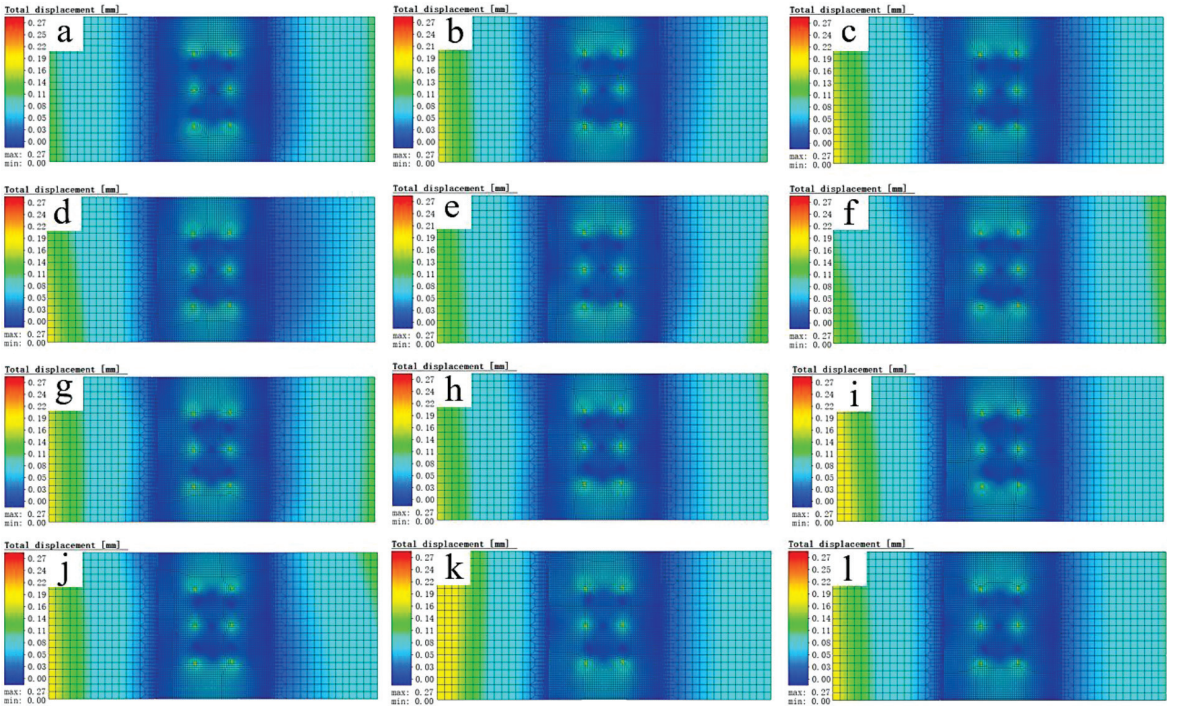

Figure 6: Numerical simulation results of total deformation distribution: (a-l) corresponding to welding sequences in Groups 1–12, respectively

ure 5, the welding sequence for Group 7 (1-4-3-6-2-5) results in the lowest maximum equivalent stress after welding. In contrast, the sequence for Group 5 (2-1-3-5-6-4) produces the highest maximum equivalent stress. Therefore, from the perspective of post-welding equivalent stress, the welding sequence for Group 7 (1-4-3-6-2-5) is the optimal sequence.

The welding pattern for Group 7 involves first cross-welding the four outermost spots diagonally, followed by welding the two central spots. In contrast, Group 5's welding pattern starts with the two central spots, followed by the four outer spots. Therefore, in actual equally spaced laser spot welding applications, welding the central spots first, followed by the side spots, is not recommended. By implementing cross-welding of diagonal spots first, followed by central spots, the residual stress in welded components can be significantly reduced.

The total deformation simulation results are presented in **Figure 6**. As shown in this figure, the maximum total deformation values for all twelve welding sequences are identical at 0.27 mm. Significant deformation occurs around the weld spots. In contrast, deformation in areas outside the weld spots throughout the lap joint is minimal and negligible. Consequently, the welding sequence exhibits minimal influence on the total joint deformation, highlighting key advantages of laser spot welding including a concentrated energy input and a limited heat-affected zone.

A comparison of **Figures 5** and **6** reveals a notable phenomenon: under a constant fixture clamping force, the laser spot welding sequence significantly influences the maximum equivalent stress in the welded part, and yet it has a negligible effect on the maximum total deformation. Specifically, the maximum total deformation remains constant at 0.27 mm across all welding sequences. The reasons for this phenomenon can be summarized as follows:

(1) Highly localized energy input. Laser spot welding delivers a highly concentrated energy input, resulting in a small heat-affected zone. Consequently, deformation is primarily localized near the weld spots. Since the total heat input to the entire structure is not substantially altered by the welding sequence, the resulting deformation exhibits minimal variation.

(2) Rigid fixture constraints. The sheet was subjected to rigid constraints from the fixture (with a clamping force of 100 N) on both sides. These constraints effectively suppress the overall warping or bending deformation (macroscopic deformation) of the workpiece. Therefore, despite variations in the internal stress distribution induced by the welding sequence, the fixture confines the overall deformation of the workpiece to a minimal range.

(3) Distinct influencing factors for stress and deformation. Stress arises from the accumulation of internal forces due to constrained deformation and uneven cooling. Thus, the welding sequence significantly affects the interaction and balance of these localized stresses. In contrast, total deformation characterizes the macroscopic shape change of the entire sheet. Under identical conditions – including fixture constraint force, number of weld spots, and their distribution – the final overall deformation remains consistent.

4.2 Comparative analysis of laser spot welding simulation results under varied fixture clamping forces

As demonstrated in Section 4.1, Group 7's welding sequence (1-4-3-6-2-5) yields the minimum post-welding residual stress, establishing it as the optimal welding configuration. Based on this finding, Group 7's welding sequence was employed in numerical simulations. Fixture clamping forces were systematically varied to investigate their influence on the post-welding residual stress and deformation characteristics. Six additional simulation groups (Groups 13–18) were designed. **Table 6** details the corresponding fixture clamping forces for these experimental group.

Table 6: Applied fixture clamping forces across experimental groups (Groups 13–18)

Group	13	14	15	16	17	18
Clamping force (N)	80	90	95	100	105	110

Simulation results of the equivalent stress and total deformation for Groups 13–18 are shown in **Figure 7**. Statistical analysis of the maximum values of the equivalent stress and total deformation across different groups was performed, and the results are summarized in **Figure 8**. As shown in this figure, Group 16 demonstrates the lowest values for both the maximum equivalent stress and maximum total deformation. Therefore, the 100 N clamping force used for Group 16 is identified as the optimal fixture clamping force.

Based on the analysis of the optimal welding sequence presented in Section 4.1, the following conclusion is drawn: The optimal laser spot welding process for 304 austenitic stainless steel thin plates involves conducting the welding process with a clamping force of 100 N applied to fixtures on both sides, while implementing a welding sequence (1-4-3-6-2-5) that begins with cross-welding the four outermost welding spots diagonally, followed by welding the two middle welding spots.

The above simulation results indicate that the laser spot welding sequence and fixture clamping force have significant effects on the equivalent stress and deformation of the welded parts. In this study, the optimal welding sequence and fixture clamping force were determined based on the simulation results. Meanwhile, Gannon et al.[43] used ANSYS software to simulate the influence of welding sequences on the residual stress and deformation of flat steel stiffened plates and found that the deformation and residual stress induced by cross welding were the smallest. Geng et al.[44] found through experimental and numerical simulation methods that adopting the End?Middle?End path effectively reduced welding residual deformation. The research results of the above two scholars are consistent with the optimal welding sequence obtained in this study, which indirectly validates the reliability of the numerical simulation results presented in this paper.

Analysis of simulation results regarding equivalent stress and deformation in the weld spot region

To better visualize the distribution of stress and strain around a laser weld spot, a weld spot from the simulation

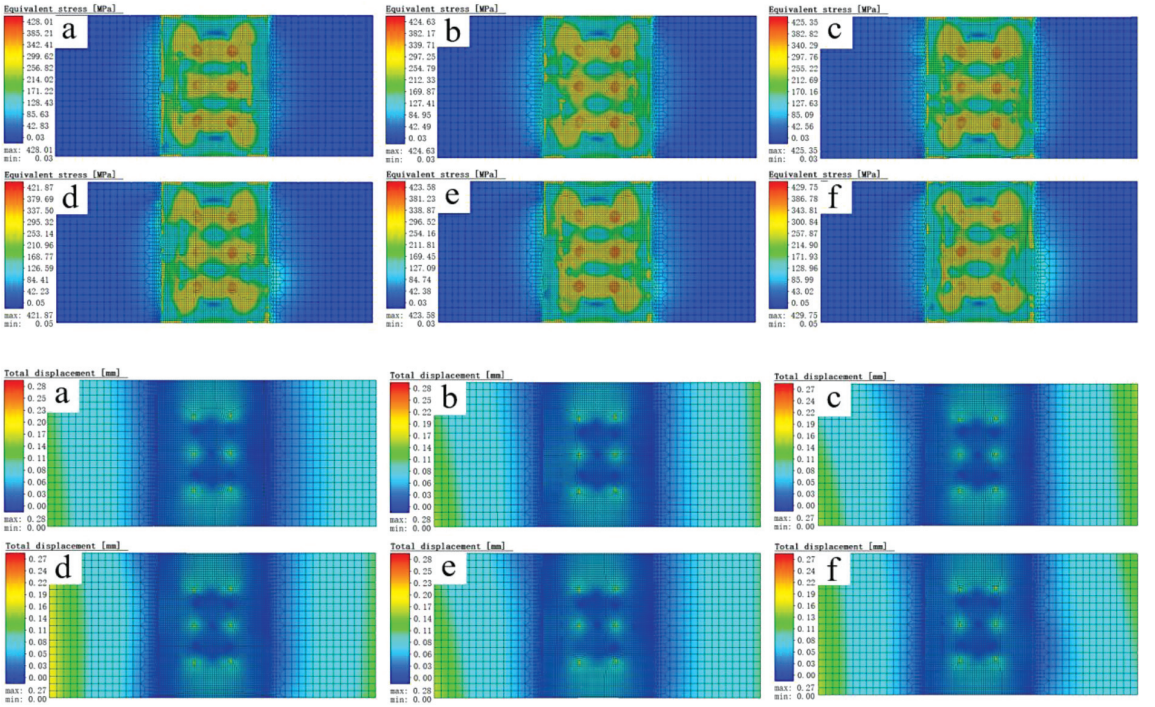

Figure 7: Equivalent stress and total deformation distribution from numerical simulations: (a–f) corresponding to fixture clamping force in Groups 13–18, respectively

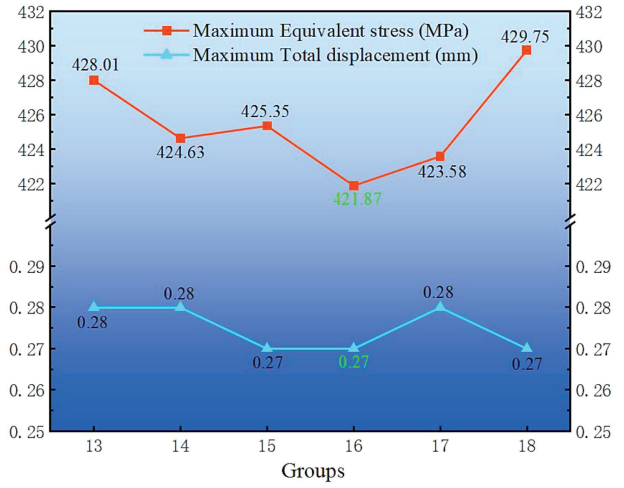

Figure 8: Statistical results of the maximum equivalent stress and maximum total deformation under different fixture clamping forces

results of Group 7 (the optimal welding process group) was selected. 3D distribution maps of equivalent stress and total deformation around the weld spot were plotted, as shown in **Figure 9**.

As shown in this figure, the peak values of both equivalent stress and total deformation are concentrated at the center of the weld spot, indicating the maximum values for both parameters. Radially outward from the weld spot center, both equivalent stress and total deformation decrease gradually in a concentric pattern. The gradient of both equivalent stress and total deformation is steeper in proximal regions compared to the gentler

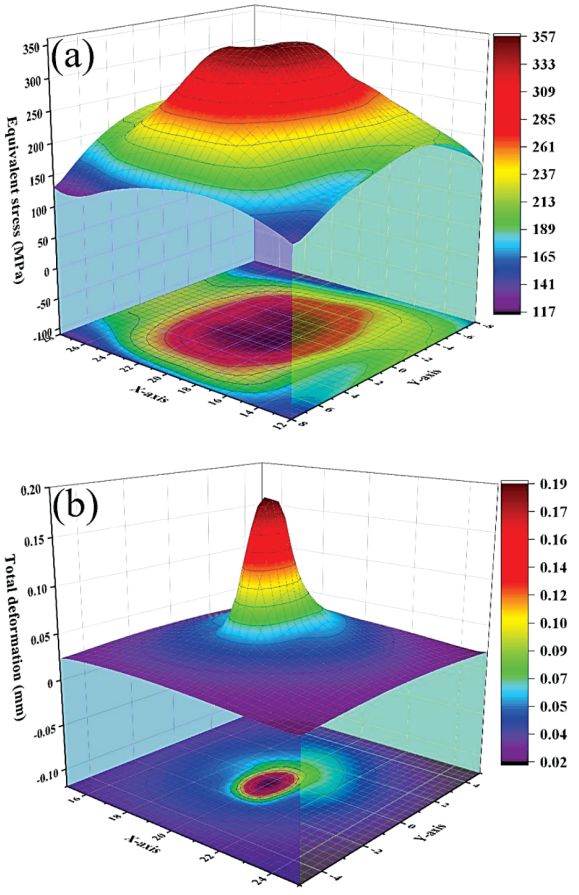

Figure 9: Three-dimensional distribution maps of (a) equivalent stress and (b) total deformation in the vicinity of the weld spot

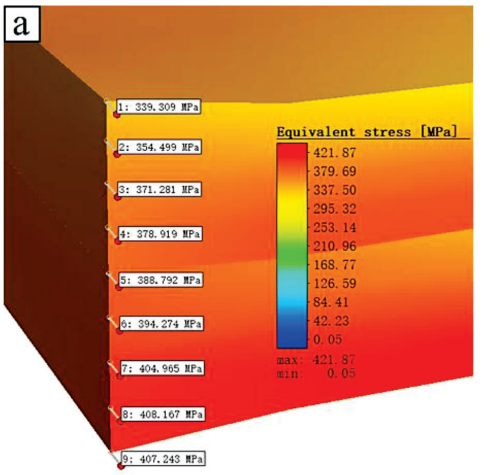

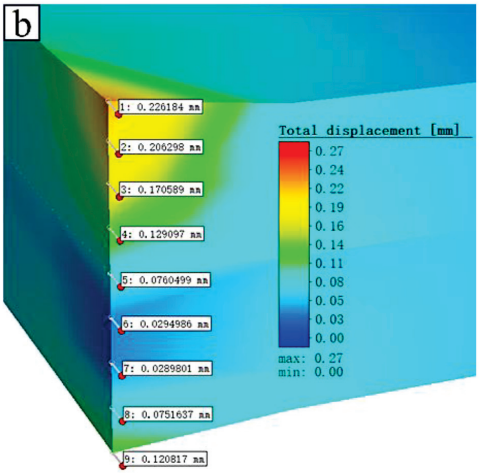

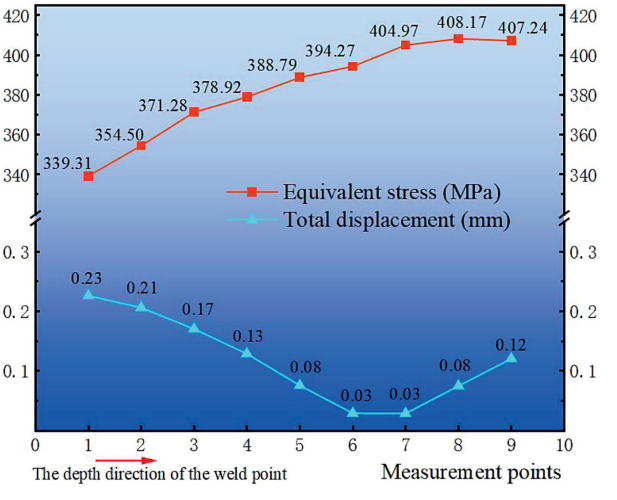

Figure 10: Cross-sectional analysis through weld spot center: (a) equivalent stress distribution, (b) total deformation profile and variation curves

slope in distal regions, indicating that the rate of decrease is faster near the weld center.

The bottom projection map shows that the equivalent stress has a wider distribution range compared to the deformation. Furthermore, the deformation equipotential lines maintain a closed configuration. In contrast, the equivalent stress equipotential lines transition from closed in proximal zones to open in distal zones. This phenomenon is due to the extensive distribution range of the equivalent stress and the mutual interaction between adjacent weld spots. The distal equivalent stress equipotential lines are interconnected with those of the neighboring weld spots. Consequently, they appear as non-closed lines in the single weld spot projection map.

Based on the preceding analysis, the peak values of both equivalent stress and total deformation are concentrated at the weld spot. To further investigate the distribution of stress and strain along the depth axis of the weld spot region, a cross-sectional analysis was performed. Nine measurement points were established along the depth direction (z-axis) to evaluate the variations in the equivalent stress and total deformation, as shown in **Figure 10**. The equivalent stress and deformation data for these measurement points were statistically analyzed. As shown in the variation curves (**Figure 10**), the equivalent stress increases with the weld spot depth. The total deformation shows a non-monotonic variation, decreasing initially and then increasing along the depth direction. The deformation magnitude at the weld spot top surface (0.23 mm) is significantly greater than that at the bottom surface (0.12 mm). The reason for the observed variation in the equivalent stress is that the energy of the conical heat source model gradually decreases from top to bottom, leading to progressively smaller heat input in the depth direction of the welding spot. The lower heat input leads to a higher cooling rate, generating larger residual stresses.[45,46]

5 CONCLUSIONS

This study investigated the laser spot welding of 304 austenitic stainless steel thin plates through numerical simulations performed using Simufact Welding software. The research focused on analyzing the effects of the welding sequence and fixture clamping force on the post-welding residual stress and deformation, leading to the optimization of process parameters for 304 stainless steel thin plate welding. The key findings are summarized as follows:

(1) The welding sequence significantly affects the residual stress distribution in welded joints. The optimal pattern involves diagonal cross-welding of the four outermost welding spots, followed by welding the two middle welding spots (1-4-3-6-2-5). This sequence minimizes the maximum equivalent stress to 421.87 MPa, establishing it as the optimal welding sequence.

(2) The total post-welding deformation values from simulations under different welding sequences were essentially identical. This suggests that the welding sequence has a relatively minor influence on the total post-welding deformation in laser spot-welded 304 stainless steel thin plates.

(3) Under the optimal welding sequence, with 100 N clamping forces applied by the fixtures on both sides, the maximum equivalent stress and the maximum total post-welding deformation reach the minimum values of 421.87 MPa and 0.27 mm, respectively.

(4) Both the equivalent stress and total deformation reach peak values at the welding spot center. The values decrease with increasing distance from the welding spot, with a more pronounced rate of decrease near the welding spot. In the depth direction, the equivalent stress exhibits a gradually increasing trend, while the total deformation initially decreases and then increases. The deformation magnitude at the welding spot top surface exceeds that at the bottom surface.

(5) The optimal process parameters for the laser spot welding of 304 austenitic stainless steel thin plates are a clamping force of 100 N and a welding sequence (1-4-3-6-2-5), minimizing the residual stress and deformation.

Acknowledgments

This work was supported by the Henan Province Science and Technology Research and Development Joint Fund (Industry Category): Key Technology Research and Industrialization of High Speed Oil Free Lubrication Shaft Pump and Motor for Hydrogen Use (No. 225101610002), Key Scientific Research Projects of Higher Education Institutions in the Henan Province (No. 24A460017), Key R & D and Promotion Project of the Henan Province (Science and Technology Research) (No. 252102220064), Key R & D and Promotion Project of the Henan Province (Science and Technology Research) (No. 262102220041).

6 REFERENCES

[1] C. Lv, Y. Liu, D. Suo, K. Zheng, Y. Sun, J. Li, Y. Jiang, Effect of ultraviolet illumination on corrosion resistance of 304 austenitic stainless steel in molybdate-containing solution, J Mater Res Technol, 28 (**2024**), 1263–1275, doi:10.1016/j.jmrt.2023.12.058

[2] X. Chen, C. Zhou, J. Zheng, L. Zhang, Effects of α' martensite and deformation twin on hydrogen-assisted fatigue crack growth in cold/warm-rolled type 304 stainless steel, Int J Hydrogen Energy, 43 (**2018**), 3342–3352, doi:10.1016/j.ijhydene.2017.12.173

[3] X. Lan, B. Hu, S. Wang, W. Luo, P. Fu, Magnetic characteristics and mechanism of 304 austenitic stainless steel under fatigue loading, Eng Fail Anal, 136 (**2022**), 106182, doi:10.1016/j.engfailanal.2022.106182

[4] D. P'ng, P. Molian, Q-switch Nd:YAG laser welding of AISI 304 stainless steel foils, Mater Sci Eng A, 486 (**2008**), 680–685, doi:10.1016/j.msea.2007.08.063

[5] R. Ren, X. Ma, H. Yue, F. Yang, Y. Lu, Stiffness enhancement methods for thin-walled aircraft structures: A review, Thin-Walled Struct, 201 (**2024**), 111995, doi:10.1016/j.tws.2024.111995

[6] S. T. Mekonone, T. G. Gemechu, T. H. Mekonnen, A. M. Momhur, Optimization, thermo-mechanical loading effects and microstructure evolutions of Metal Inert Gas (MIG) welded 304L stainless steel, Mater Today Commun, 42 (**2025**), 111514, doi:10.1016/j.mtcomm.2025.111514

[7] C. Zhou, P. Dai, H. Wu, M. He, X. Liu, P. K. Chu, Effect of the ferrite morphology on hydrogen embrittlement of MAG welded 304 austenitic stainless steel, Appl Surf Sci, 606 (**2022**), 154866, doi:10.1016/j.apsusc.2022.154866

[8] P. V. S. S. Sridhar, P. Biswas, P. Mahanta, Influence of welding current on bead profile and mechanical properties of double sided submerged arc welding of AISI 304 austenitic stainless steel, Mater Today: Proc, 19 (**2019**), 831–836, doi:10.1016/j.matpr.2019.08.140

[9] J. Sun, K. Dilger, Influence of welding sequence and external restraint on buckling distortion in thin-plate arc-welded joints, J Adv Joining Processes, 8 (**2023**), 100157, doi:10.1016/j.jajp.2023.100157

[10] C. Liu, Z. Luo, J. Zheng, Y. He, S. Huang, H. Ding, G. Shen, Numerical analysis of the formation mechanism of high back penetration depth of thin plate aluminum alloy in MIG welding, Appl Therm Eng, 262 (**2025**), 125264, doi:10.1016/j.applthermaleng.2024.125264

[11] Y. Qiu, R. Yan, N. Wang, W. Shen, S. Xu, M. Li, K. Qin, Stress amplification effect and fatigue strength evaluation of marine thin plate welded structure considering welding deformation: Theoretical and experimental analysis, Thin-Walled Struct, 188 (**2023**), 110871, doi:10.1016/j.tws.2023.110871

[12] L. Ding, Q. Lu, S. Liu, R. Xu, X. Yan, X. Xu, M. Lu, Y. Chen, Quality inspection of micro solder joints in laser spot welding by laser ultrasonic method, Ultrasonics, 118 (**2022**), 106567, doi:10.1016/j.ultras.2021.106567

[13] J. Zhao, K. Zeng, Numerical Simulation and Fatigue Properties of Laser Spot Weld-Bonding DP590 Dual-Phase Steel Joints, Mater Trans, 62 (**2021**), 1118–1123, doi:10.2320/matertrans.MT-M2021029

[14] Y. S. Yang, S. H. Lee, A study on the joining strength of laser spot welding for automotive applications, J Mater Process Technol, 94 (**1999**), 151–156, doi:10.1016/S0924-0136(99)00094-1

[15] L. Quintino, A. Costa, R. Miranda, D. Yapp, V. Kumar, C. J. Kong, Welding with high power fiber lasers – A preliminary study, Mater Des, 28 (**2007**), 1231–1237, doi:10.1016/j.matdes.2006.01.009

[16] Z. Wu, J. Wan, Y. Zhang, C. Li, Y. Liu, C. Yang, The influence of welding speed on nanosecond laser welding of AZ31B magnesium alloy and 304 stainless steel, Opt Laser Technol, 168 (**2024**), 109997, doi:10.1016/j.optlastec.2023.109997

[17] T. R. Allen, T. G. Fleming, T. J. H. Krause, J. M. Fraser, Simultaneous high-speed keyhole depth and absorptance measurements in laser spot welding of dissimilar metals, Procedia CIRP, 111 (**2022**), 5–9, doi:10.1016/j.procir.2022.08.041

[18] H. Lapsanska, H. Chmelickova, M. Hrabovsky, Effect of Beam Energy on Weld Geometric Characteristics in Nd:YAG Laser Overlapping Spot Welding of Thin AISI 304 Stainless Steel Sheets, Metall Mater Trans B, 41 (**2010**), 1108–1115, doi:10.1007/s11663-010-9399-8

[19] H. Li, Q. Yao, X. Wang, H. Liu, CFD numerical simulation of melt flow and weld pool formation in semiconductor laser direct welding of 6061 aluminium alloy with PET based on surface microtextured, Opt Laser Technol, 183 (**2025**), 112236, doi:10.1016/j.optlastec.2024.112236

[20] W. Zhou, Q. Le, Y. Shi, Q. Liao, Z. Yin, Y. Jiang, Numerical simulation of gas tungsten arc welding for ZW61 magnesium alloy thin plates, Mater Chem Phys, 329 (**2025**), 130130, doi:10.1016/j.matchemphys.2024.130130

[21] X. Fan, G. Qin, Z. Jiang, H. Wang, Comparative analysis between the laser beam welding and low current pulsed GMA assisted high-power laser welding by numerical simulation, J Mater Res Technol, 22 (**20**23), 2549–2565, doi:10.1016/j.jmrt.2022.12.116

[22] P. Xia, C. Wang, G. Mi, M. Zhang, L. Xiong, X. Zhang, C. Zhai, X. Feng, Y. Hu, Numerical simulation of molten pool flow behavior and keyhole evolution behavior in dual-laser beam oscillating bilateral synchronous welding of T-joints, Int J Heat Mass Transfer, 209 (**2023**), 124114, doi:10.1016/j.ijheatmasstransfer.2023.124114

[23] Z. Wang, M. Gao, Numerical simulations of oscillating laser welding: A review, J Manuf Processes, 119 (**2024**), 744–757, doi:10.1016/j.jmapro.2024.04.001

[24] A. Zarei, M. Akbari, A. Abdollahi, H. Soleimanimehr, Experimental and numerical study of dissimilar fiber laser welding of martensitic AISI 1060 carbon steel with different configuration with austenitic 304 and ferritic 420 stainless steel, Heliyon, 10 (**2024**), e39954, doi:10.1016/j.heliyon.2024.e39954

[25] H. Danielewski, A. Skrzypczyk, M. Hebda, S. Tofil, G. Witkowski, P. Dlugosz, R. Nigrovic, Numerical and Metallurgical Analysis of Laser Welded, Sealed Lap Joints of S355J2 and 316L Steels under Different Configurations, Mater, 13 (**2020**), doi:10.3390/ma13245819

[26] H. Lebbal, M. Chaib, A. Slimane, D. Ait Kaci, N. Boualem, Experimental Investigation with Optimization of Spot Welding Parameters on Stainless Steel AISI 304, JOM, 75 (**2023**), 4993–5002, doi:10.1007/s11837-023-06136-3

[27] D. Rajesh, V. Chandran, N. Lenin, A. Subramanian, M. Deva, P. Balamurugan, Optimization of dual pulse resistance welding parameters for ASTM A240 stainless steel sheets: a multi-objective approach, Interactions, 245 (**2024**), 140, doi:10.1007/s10751-024-01992-0

[28] Y. Cui, W. Wang, H. Wang, B. Li, P. Zhao, F. Xuan, Cyclic behavior and damage mechanism of 304 austenitic stainless steel under different control modes, J Mater Res Technol, 30 (**2024**), 854–865, doi:10.1016/j.jmrt.2024.03.114

[29] N.-K. Wei, J. Shi, R.-D. Yang, J.-T. Xi, X.-M. Luo, X.-Y. Yin, R.-X. Zhang, Numerical Simulation and Experimental Analysis on Seam Feature Size and Deformation for T-Joint Laser–GMAW Hybrid Welding, Mater, 17 (**2024**), doi:10.3390/ma17010228

[30] A. K. Unni, M. Vasudevan, Determination of heat source model for simulating full penetration laser welding of 316 LN stainless steel by computational fluid dynamics, Mater Today: Proc, 45 (**2021**), 4465–4471, doi:10.1016/j.matpr.2020.12.842

[31] T. Kik, Heat Source Models in Numerical Simulations of Laser Welding, Mater, 13 (2020), doi:10.3390/ma13112653

[32] S. X. Hu, F. Li, P. Zuo, Numerical Simulation of Laser Transmission Welding–A Review on Temperature Field, Stress Field, Melt Flow Field, and Thermal Degradation, Polym, 15 (**2023**), doi:10.3390/polym15092125

[33] J. Liu, T. Jiang, Y. Shi, H. Zhu, Y. Dai, Numerical Simulation and Experimental Verification of Laser Multi-Section Welding, Chin J Mech Eng, 35 (**2022**), 125, doi:10.1186/s10033-022-00797-y

[34] J. Zhang, M. H. R. Dehkordi, M. J. Kholoud, H. Azimy, S. Daneshmand, Experimental and numerical study of melt flow, temperature behavior and heat transfer mechanisms during the dissimilar laser welding process, Opt Laser Technol, 180 (**2025**), 111521, doi:10.1016/j.optlastec.2024.111521

[35] Y. Zhang, A. M. Alqahtani, Y. Qiu, A. M. A. Elsiddieg, T. Saidani, A. G. Alkhathami, Finite volume modeling and experimental analysis of keyhole dynamics, temperature field and weld characterizations of Ti-6Al-4V tubes with unequal thickness in fiber laser welding, Opt Laser Technol, 192 (**2025**), 113778, doi:10.1016/j.optlastec.2025.113778

[36] N. Siva Shanmugam, G. Buvanashekaran, K. Sankaranarayanasamy, Some studies on weld bead geometries for laser spot welding process using finite element analysis, Mater Des, 34 (**2012**), 412–426, doi:10.1016/j.matdes.2011.08.005

[37] K. P. Prajadhiana, Y. H. P. Manurung, A. Bauer, M. S. Adenan, N. I. Syahriah, M. A. Mohamed, B. Awiszus, M. Graf, A. Haelsig, Experi-

mental verification of computational and sensitivity analysis on substrate deformation and plastic strain induced by hollow thin-walled WAAM structure, Rapid Prototyping J, 28 (**2021**), 559–572, doi:10.1108/rpj-06-2020-0135

[38] H. Huang, J. Wang, L. Li, N. Ma, Prediction of laser welding induced deformation in thin sheets by efficient numerical modeling, J Mater Process Technol, 227 (**2016**), 117–128, doi:10.1016/j.jmatprotec.2015.08.002

[39] A. Shah, A. Kumar, J. Ramkumar, Analysis of transient thermo-fluidic behavior of melt pool during spot laser welding of 304 stainless-steel, J Mater Process Technol, 256 (**2018**), 109–120, doi:10.1016/j.jmatprotec.2018.02.005

[40] W. Zhu, F. Tang, Y. Ren, X. Yang, Y. Xu, Y. Xu, Influence of the residual welding stress on the corrosion propagation of the steel cages of the CRTS slabs in the high-speed railway, Constr Build Mater, 458 (**2025**), 139336, doi:10.1016/j.conbuildmat.2024.139336

[41] Y. Guo, Y. Teng, G. Liu, T. Jiao, Numerical study on creep-fatigue damage of titanium alloy pressure shell considering the effect of welding residual stresses, Thin-Walled Struct, 209 (**2025**), 112953, doi:10.1016/j.tws.2025.112953

[42] W. Sun, Y. Xia, M. Chen, G. Fan, A study on the role of local residual stress on the local strength and defect growth in laser-welded Ti-6Al-4V, J Alloys Compd, 1018 (**2025**), 179174, doi:10.1016/j.jallcom.2025.179174

[43] L. Gannon, Y. Liu, N. Pegg, M. Smith, Effect of welding sequence on residual stress and distortion in flat-bar stiffened plates, Marine Structures, 23 (**2010**), 385–404, doi:10.1016/j.marstruc.2010.05.002

[44] S. Geng, Y. Li, P. Jiang, Y. Wang, J. Jin, C. Han, Influence of welding sequences on residual stress and deformation of U-rib components fabricated by laser-arc hybrid welding, Journal of Materials Research and Technology, 35 (**2025**), 726–742, doi:10.1016/j.jmrt.2025.01.032

[45] A. Kumar, S. M. Pandey, S. Sirohi, D. Fydrych, C. Pandey, P92 steel and inconel 617 alloy welds joint produced using ERNiCr-3 filler with GTAW process: Solidification mechanism, microstructure, mechanical properties and residual stresses, Heliyon, 9 (**2023**), e18959, doi:10.1016/j.heliyon.2023.e18959

[46] D. Guo, K. Yan, M. D. Callaghan, D. Daisenberger, M. Chatterton, J. Chen, A. Wisbey, W. Mirihanage, Solidification microstructure and residual stress correlations in direct energy deposited type 316L stainless steel, Mater Des, 207 (**2021**), 109782, doi:10.1016/j.matdes.2021.109782